

Dynamic intracellular exchange of nanomaterials' protein corona perturbs proteostasis and remodels cell metabolism

Cai, Rong; Ren, Jiayu; Guo, Mengyu; Wei, Taotao; Liu, Ying; Xie, Chunyu; Zhang, Peng; Guo, Zhiling; Chetwynd, Andy; Lynch, Iseult; Ke, Pu Chun ; Chen, Chunying

DOI:

[10.1073/pnas.2200363119](https://doi.org/10.1073/pnas.2200363119)

License:

Creative Commons: Attribution-NonCommercial-NoDerivs (CC BY-NC-ND)

Document Version

Publisher's PDF, also known as Version of record

Citation for published version (Harvard):

Cai, R, Ren, J, Guo, M, Wei, T, Liu, Y, Xie, C, Zhang, P, Guo, Z, Chetwynd, A, Lynch, I, Ke, PC & Chen, C 2022, 'Dynamic intracellular exchange of nanomaterials' protein corona perturbs proteostasis and remodels cell metabolism', *Proceedings of the National Academy of Sciences of the United States of America*, vol. 119, no. 23, e2200363119. <https://doi.org/10.1073/pnas.2200363119>

[Link to publication on Research at Birmingham portal](#)

General rights

Unless a licence is specified above, all rights (including copyright and moral rights) in this document are retained by the authors and/or the copyright holders. The express permission of the copyright holder must be obtained for any use of this material other than for purposes permitted by law.

- Users may freely distribute the URL that is used to identify this publication.
- Users may download and/or print one copy of the publication from the University of Birmingham research portal for the purpose of private study or non-commercial research.
- User may use extracts from the document in line with the concept of 'fair dealing' under the Copyright, Designs and Patents Act 1988 (?)
- Users may not further distribute the material nor use it for the purposes of commercial gain.

Where a licence is displayed above, please note the terms and conditions of the licence govern your use of this document.

When citing, please reference the published version.

Take down policy

While the University of Birmingham exercises care and attention in making items available there are rare occasions when an item has been uploaded in error or has been deemed to be commercially or otherwise sensitive.

If you believe that this is the case for this document, please contact UBIRA@lists.bham.ac.uk providing details and we will remove access to the work immediately and investigate.



Dynamic intracellular exchange of nanomaterials' protein corona perturbs proteostasis and remodels cell metabolism

Rong Cai^{a,b,1}, Jiayu Ren^{a,b,c,1}, Mengyu Guo^{a,b}, Taotao Wei^d, Ying Liu^{a,b,c,e}, Chunyu Xie^{a,b,c}, Peng Zhang^f, Zhiling Guo^f, Andrew J. Chetwynd^f, Pu Chun Ke^e, Iseult Lynch^f, and Chunying Chen^{a,b,c,e,2}

Edited by Catherine Murphy, University of Illinois at Urbana–Champaign, Urbana, IL; received January 9, 2022; accepted April 7, 2022

The nanomaterial–protein “corona” is a dynamic entity providing a synthetic–natural interface mediating cellular uptake and subcellular distribution of nanomaterials in biological systems. As nanomaterials are central to the safe-by-design of future nanomedicines and the practice of nanosafety, understanding and delineating the biological and toxicological signatures of the ubiquitous nanomaterial–protein corona are precursors to the continued development of nano–bio science and engineering. However, despite well over a decade of extensive research, the dynamics of intracellular release or exchange of the blood protein corona from nanomaterials following their cellular internalization remains unclear, and the biological footprints of the nanoparticle–protein corona traversing cellular compartments are even less well understood. To address this crucial bottleneck, the current work screened evolution of the intracellular protein corona along the endocytotic pathway from blood via lysosomes to cytoplasm in cancer cells. Intercellular proteins, including pyruvate kinase M2 (PKM2), and chaperones, displaced some of the initially adsorbed blood proteins from the nanoparticle surface, which perturbed proteostasis and subsequently incited chaperone-mediated autophagy (CMA) to disrupt the key cellular metabolism pathway, including glycolysis and lipid metabolism. Since proteostasis is key to the sustainability of cell function, its collapse and the resulting CMA overdrive spell subsequent cell death and aging. Our findings shed light on the consequences of the transport of extracellular proteins by nanoparticles on cell metabolism.

protein corona | proteostasis | chaperone-mediated autophagy | cell metabolism

When nanomaterials (NMs) enter a biological fluid, the biomolecules in presence rapidly bind to the surface of the NMs to form a “biomolecular corona” (1). The corona paradigm has been established since 2007 (2, 3), underscoring the acquired biological identity of engineered NMs and impacting the therapeutic efficacy (4) and safety of NMs as well as their biological behaviors, including cell recognition (5–7), ligand targeting efficacy (8, 9), biodistribution (10, 11), immune modulation (12–15), and toxicity (16–19).

Most of the current biomolecular corona studies have focused on the blood plasma/serum, where immunoglobulins, apolipoproteins, complements, and coagulation cascade biomolecules are enriched on the nanoparticle surface and critically affect the nanoparticle-entailed pathophysiology and toxicity downstream (5–7, 20). However, most targets of NMs for biomedical applications are at the subcellular level (21–25), and thus, understanding NMs involvement in intracellular events is important to ensure their therapeutic efficacy (4). To date, limited efforts have been devoted to delineating the uptake routes, and very few studies have focused on the molecular cell biology once the corona-coated NMs become resident in cells and/or tissues. It is already known that the corona on polymer-coated NMs can exchange with other biomolecules that are both internal and external to the cell (26). The nanoparticle–intracellular protein entities can regulate the macrophage phenotype and induce a stress response of the endothelium (27). However, nano–bio interactions occurring within the cell are still considered a “black box” in terms of the physiological responses to NMs exposure (28–31) due to the complexity and technical challenges involved in interrogating cellular response to a dynamic nanoparticle–protein corona.

To clarify the biochemical properties of the intracellular protein corona, three aspects need to be examined: 1) profile of the intracellular protein corona, which is determined by the nature of cytoplasmic fluids; 2) evolution of the protein corona along the entire delivery process from blood to subcellular sites of the target; and 3) cryptic epitopes formed at the new nanoprotein interface that may trigger inappropriate cell signaling events. It is well known that cellular protein profiles need to be

Significance

This study analyzed the dynamic protein corona on the surface of nanoparticles as they traversed from blood to cell lysosomes and escaped from lysosomes to cytoplasm in the target cells. We found with proteomic analysis an abundance of chaperone and glycolysis coronal proteins (i.e., heat shock cognate protein 70, heat shock protein 90, and pyruvate kinase M2 [PKM2]) after escape of the nanoparticles from lysosomes to the cytosol. Alterations of the coronal proteins (e.g., PKM2 and chaperone binding) induced proteostasis collapse, which subsequently led to elevated chaperone-mediated autophagy (CMA) activity in cells. As PKM2 is a key molecule in cell metabolism, we also revealed that PKM2 depletion was causative to CMA-induced cell metabolism disruption from glycolysis to lipid metabolism.

Author contributions: C.C. designed research; R.C., J.R., M.G., C.X., and C.C. performed research; R.C., J.R., Y.L., and C.C. analyzed data; T.W., P.Z., Z.G., A.J.C., P.C.K., and I.L. edited the manuscript; and R.C., J.R., T.W., Z.G., A.J.C., P.C.K., I.L., and C.C. wrote the paper.

The authors declare no competing interest.

This article is a PNAS Direct Submission.

Copyright © 2022 the Author(s). Published by PNAS. This article is distributed under [Creative Commons Attribution-NonCommercial-NoDerivatives License 4.0 \(CC BY-NC-ND\)](https://creativecommons.org/licenses/by-nc-nd/4.0/).

¹R.C. and J.R. contributed equally to this work.

²To whom correspondence may be addressed. Email: chenchy@nanoctr.cn.

This article contains supporting information online at [http://www.pnas.org/lookup/suppl/doi:10.1073/pnas.2200363119/-DCSupplemental](https://www.pnas.org/lookup/suppl/doi:10.1073/pnas.2200363119/-DCSupplemental).

Published June 2, 2022.

controlled to maintain protein homeostasis (proteostasis) when cells are subjected to unique stresses in the local environments (32, 33).

In this study, we hypothesized that the transport of adsorbed proteins (the protein corona) by NMs from outside of cells and the release of blood proteins inside the cells due to exchange with intracellular proteins may disturb cellular proteostasis, causing aberrant protein stress and perturbation of cellular biological behaviors. We found that the protein corona evolved significantly from the plasma migrating to lysosomal fluids and subsequent cytosolic fluids while retaining some fingerprints of their initial characteristics corona to induce intracellular proteostasis collapse. The cytosolic pyruvate kinase isoform M2 (PKM2) and chaperones, including heat shock cognate protein 70 (HSC70) and heat shock protein 90 (HSP90), were exchanged onto the surface of the protein corona along the endocytotic pathway. This newly formed nanoprotein interaction up-regulated chaperone-mediated autophagy (CMA) activity in cells and subsequently disrupted cell metabolism, including glycolysis and lipid metabolism. This study suggests that it is the intracellular protein corona on the NM surface, acquired during the dynamic evolution process along the transport from plasma to subcellular spaces, rather than the initial corona formed in plasma that dominates subcellular localization of NMs and their physiological processes.

Evolution of the Intracellular Protein Corona along the Endocytosis Pathway

To establish the dynamic intracellular protein corona of NMs, we prepared spherical gold nanoparticles (GNPs) as a model material (34) (*SI Appendix, Fig. S1*) and profiled the composition of their adsorbed proteins along the endocytotic pathway as shown in Fig. 1. Transmission electron microscopy (TEM) images revealed the mean size of GNPs to be 13.0 ± 1.0 nm, whereas the hydrodynamic size was around 30 nm (*SI Appendix, Fig. S1 A, B, and D*). Upon protein adsorption, the zeta potential of the GNPs remained negative, but the size of GNPs increased slightly; the ultraviolet-visible spectroscopy absorbance peak displayed a significant red shift (*SI Appendix, Fig. S1 C–E*). GNPs were incubated with human blood plasma (stage I) and sequentially transferred to freshly isolated lysosomal (stage II) and cytosol extracts (stage III) from human cervical carcinoma cell line (HeLa cells) in order to mimic the internalization pathway (Fig. 1*A* and *SI Appendix, Figs. S3–S5*). We used GNP^B (gold nanoparticle blood), GNP^{BL} (gold nanoparticle blood–lysosome), and GNP^{BLC} (gold nanoparticle blood–lysosome–cytosol) to indicate the three stages of the protein corona evolution in cells. Label-free quantitative liquid chromatography–mass spectrometry (LC-MS) was employed to identify and quantify composition and evolution of the protein coronas in different biological media (*Dataset S1*). A decreasing protein amount on the surface of the GNPs in lysosomes was observed, and a slight increase of the corona (protein) amount occurred when the GNPs entered the cytosol (Fig. 1*B*). This may be due to a partial degradation of the blood plasma-derived protein corona in the lysosomes (35) during stage II or the result of exchange of plasma proteins for lysosomal/cytosolic proteins (26). As shown in the Venn diagram (Fig. 1*C*), 198, 184, and 248 proteins were found within the coronas formed on GNP^B, GNP^{BL}, and GNP^{BLC}, respectively; 172 overlapping proteins were identified, suggesting that these proteins were consistently present during the whole sequential incubation process. When the GNP^B entered lysosomes, 173 proteins remained unaltered, and 11 new lysosomal proteins

appeared on the surface of GNP^{BL}. The lower protein amount and nonspecific protein population on the surface of the GNP^{BL} suggested that a loss of corona proteins in lysosomes occurred via degradation of some blood plasma-derived proteins rather than by exchange of proteins. On the contrary, 65 cytosolic proteins were acquired in the corona on the GNP^{BLC} after the latter was isolated from lysosomal extracts and subsequently entered the cytosolic extracts, of which 22 overlapping plasma proteins were readsorbed to the particles. Detailed protein populations corresponding to the Venn diagram are listed in *SI Appendix, Table S1* and clarified according to their locations with respect to the cell. The longer the passage taken by the GNPs and the more biofluids the particles passed through along the endocytotic pathway, the greater complexity the acquired evolving corona.

According to the physiological functions of the identified proteins, they were classified as immunoglobulin, coagulation factors, apolipoproteins, complement proteins, acute-phase proteins, and tissue leakage proteins as well as other plasma and cellular components (*SI Appendix, Fig. S6A*). Among these proteins, coagulation-related proteins were the major protein cluster found in all investigated corona compositions, and fibrinogen beta chain (FIBB), fibrinogen gamma chain (FIBG), and fibrinogen alpha chain (FIBA), which are essential for blood clot formation, were the top three most abundantly bound proteins (*SI Appendix, Fig. S6B*). Apolipoproteins, required in mammals for the assembly, secretion, and transport of complex lipids, were also abundant, with APOA1, APOC1, and APOH being the most abundant (*SI Appendix, Fig. S6C*). The increase of tissue leakage protein in the corona from GNP^B (6.8%) to GNP^{BL} (11.4%) is notable; however, that value dropped to 6.4% immediately after the GNPs entering the cytosol (*SI Appendix, Fig. S6D*). There were no obvious changes in the relative abundance of each specific component for immunoglobulins, complement proteins, and acute-phase proteins in the three types of NP–corona complex (*SI Appendix, Fig. S6 E–G*). Other proteins aside from the above-mentioned functions were increased upon entry of the GNPs into the endocytotic pathway (*SI Appendix, Fig. S6H*). Furthermore, as expected, many cellular component proteins were enriched on the GNP^{BLC} (31.2%), among which chaperones (HSP90, HSC70, and other HSP members) occupied a high proportion (3.7%). It is worth noting that the content of PKM2, which participates in glycolysis, was remarkably abundant in the GNP^{BLC} (2.4%) (*SI Appendix, Fig. S6J*). A key function of chaperone proteins is to prevent proteins from misfolding, and the proteomic results indicated that abundant chaperone proteins were present in the corona of GNP^{BLC}. This implied that many proteins on the surface of nanoparticles were unfolded. In the literature, unfolded proteins in the corona have been shown as causative to the aggregation of nanoparticles (36).

The top 50 most abundant coronal proteins were arranged in the heat map and classified into three clusters (Fig. 1*D*). For cluster I, the protein content showed a decreasing trend passing from the GNP^B to the GNP^{BLC}. Specifically, fibrinogens (FIBB, FIBG, and FIBA) displayed the most obvious downward trends (Fig. 1*E*). Signaling pathway analysis revealed that most proteins in the corona were related to the formation of fibrin clot (Fig. 1*H*). The protein concentrations in cluster II gradually increased as the particles transited from lysosomal to cytosolic solutions. These were mainly cellular component proteins, and the changes mainly occurred during the passage of GNPs from lysosomal to cytosolic extracts (Fig. 1*F*). Most of the acquired proteins were

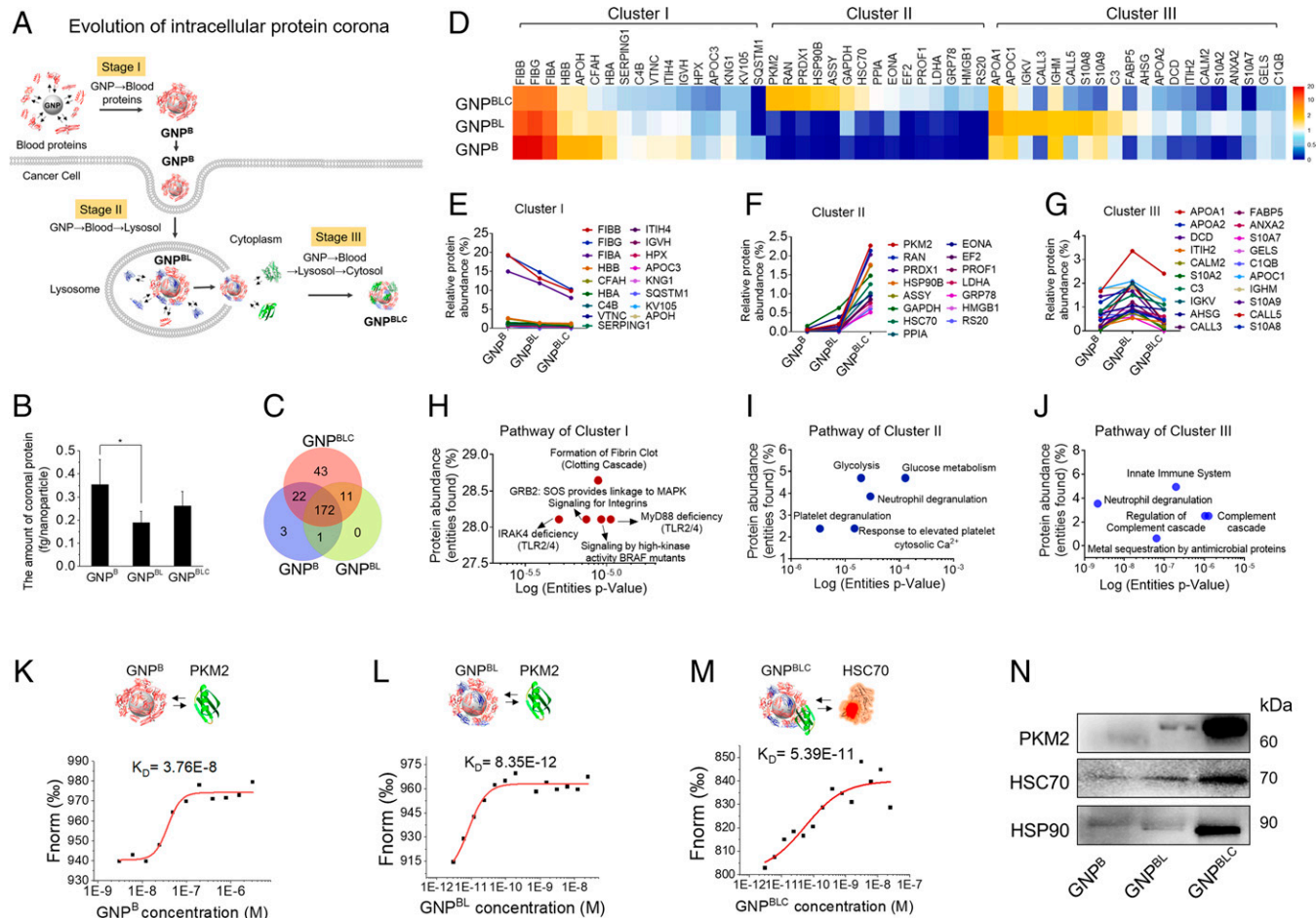


Fig. 1. Evolution of intracellular protein coronas along the endocytotic pathway. (A) Schematic representation of evolution of the protein corona along the endocytotic pathway. GNP^B, GNP^{BL}, and GNP^{BLC} indicate blood plasma-derived protein corona (GNP^B, stage I), a lysosome-evolved protein corona (GNP^{BL}, stage II) derived from GNP that moved from blood to lysosome, and a cytosolic protein corona (GNP^{BLC}, stage III) derived from GNP that escaped from the lysosomes, respectively. Proteins were identified from the Protein Data Bank (<https://www.rcsb.org/>). (B) Quantification (protein femtomogram [fg] per particle) of the protein amount within the three specific protein coronas. Data are shown as mean \pm SD from triplicates. Proteins identified in the respective nanoparticle coronas by LC-MS/MS from the three different incubation conditions were grouped according to the biological process known for the blood system. * $P < 0.01$ indicates significance. (C) Venn diagram of the numbers of identified proteins on the GNP^B, GNP^{BL}, and GNP^{BLC} surfaces. Detailed values for all individual proteins are available in *SI Appendix, Table S1*. (D) Heat map of top 50 most abundant biomolecules were clustered for the three different corona compositions. Proteins were classified into three clusters according to the changing trend of protein relative abundance from GNP^B and GNP^{BL} to GNP^{BLC} (from blood to lysosol to cytosol). Among them, cluster I proteins (E) showed a trend of gradual decrease, including FIBB, FIBG, and FIBA, indicating displacement and release from the corona. (F) Cluster II proteins displayed a trend of gradual increase, which mainly involved cellular components, like PKM2, HSP90, and HSC70. (G) Cluster III proteins presented a trend of initial increase and then, decrease, indicating that some intracellular proteins with high abundance but weak affinities for the particle surfaces were lost due to the Vroman effect. (H–J) Reactome analysis of the corresponding signaling pathways for E–G, respectively. (K) The binding affinity between PKM2 and GNP^B was $K_D = 3.76\text{E-}8$ M. (L) PKM2 easily bound to the GNP^{BL} with $K_D = 8.35\text{E-}12$ M. (M) HSC70 had a strong binding affinity for GNP^{BLC}, with $K_D = 5.39\text{E-}11$ M. (N) Western blot analysis of the indicated proteins (PKM2, HSP90, and HSC70) in the adsorbed coronas of the three different GNPs.

involved in glycolysis and glucose metabolism (Fig. 1I), which are essential processes to provide energy for cellular growth. This suggests that GNP^B phagocytosis might affect the glycolysis process of cells. The concentrations of the proteins in cluster III first increased in lysosomal solutions and then decreased upon the subsequent entry of the nanoparticles to the cytosolic extracts (Fig. 1G). Innate immune system and complement pathway proteins were revealed as the major signaling pathways in which the proteins in cluster III were involved (Fig. 1J). These results suggested that the intracellular microenvironments interfered with the initial protein corona on the GNPs acquired from blood and that the release of blood proteins from the particle surface inside the cell (following their displacement by cellular components) might modulate cellular signaling and disturb subsequent physiological cellular processes. Deficiencies in proteostasis have been shown to facilitate the progression of numerous diseases, such as lysosomal storage disease, cystic fibrosis,

amyloidogenesis, as well as cancer (37–39). Consequences of blood proteins being released from the GNP corona intracellularly are explored next.

PKM2 and Chaperones Abundantly Exchanged into the Intracellular Protein Corona

To maintain cellular proteostasis, chaperones sequester selective cellular proteins and subsequently deliver them to lysosomes (40). Among identified proteins in the cytosolic corona (GNP^{BLC}), chaperones, such as HSP90, HSC70, and PKM2, are particularly interesting given their relatively high abundances in the corona (Fig. 1I and F) and their critical roles in essential physiological processes. In parallel, PKM2 was selectively identified and targeted to the lysosomes through the interaction of HSC70 as part of, for example, tumor progression (41).

Indeed, western blotting further revealed the dynamic change and enrichment of HSC70, HSP90, and PKM2 on the GNP^{BLC} (Fig. 1*M*). It is well known that protein adsorption follows the Vroman effect, whereby the most abundant proteins generally adsorb first and are gradually replaced by less abundant proteins that have a higher affinity for the nanoparticle surface. We postulated that PKM2 and the chaperones had a high affinity for the GNP^B, resulting in a remarkable increase of the protein content within the protein corona of the GNP^{BLC}. To further confirm intracellular corona evolution and binding affinity between the GNPs and their coronal proteins, microscale thermophoresis (MST) analysis was performed. The binding affinity between PKM2 and the blood plasma-derived protein corona precoated GNP^B was evaluated to be $K_D = 3.76 \times 10^{-8}$ M (Fig. 1*K*). Interestingly, the affinity between PKM2 and GNP^{BL} went up to 8.35×10^{-12} M (Fig. 1*L*), mainly because of the loss of certain coronal proteins in lysosomes (42). Thus, there is a sharp increase of PKM2 abundance in the corona after entry of the GNPs into the cytosol (GNP^{BLC}) (Fig. 1*F*), which could be further recognized by HSC70. The binding affinity between GNP^{BLC} and HSC70 was very high ($K_D = 5.39 \times 10^{-11}$ M) (Fig. 1*M*) since PKM2 is known as an HSC70-specific binding substrate containing three KFERQ-like motifs (43). Comparably, the affinity of HSC70 with GNP^B and GNP^{BL} ($K_D = 2.21 \times 10^{-9}$ M and $K_D = 6.34 \times 10^{-8}$ M) was much lower due to their lower contents of PKM2 (SI Appendix, Fig. S7). Thus, we concluded that the protein corona pattern was determined by affinity of environmental proteins for the GNP surface coronal proteins and biological fluids that the NPs encountered. HSC70 is a marker for CMA (40), which provides a hint that evolution of the protein corona may induce more CMA.

Evolution of the Intracellular Protein Corona Induces More CMA

CMA is known to contribute to sustaining the Warburg effect and lipid metabolism (41, 43). PKM2 is a cytosolic protein that regulates the rate-limiting step of glycolysis that shifts glucose metabolism from normal respiratory chain to lactate production in tumor cells (44). Thus, we postulated that evolution of the protein corona along the endolysosomal pathway of GNPs into the cells may cause abnormal regulation of the CMA activity and subsequently, remodel glycolysis and lipid metabolism of the tumor cells.

To verify our hypothesis, we examined the CMA-related responses in HeLa cells after their exposure to GNP and GNP^B (20 nM) for 24 h. The number of lysosomes within HeLa cells increased significantly after exposure to GNP^B compared with the pristine GNP treatment (Fig. 2*B*). In order to identify the role of PKM2 in corona exchange-induced enhancement of the CMA process, we analyzed expression of key CMA-related biomarkers by establishing PKM2 knockdown HeLa cells (HeLa^{-PKM} cells). In contrast to up-regulation of CMA observed, PKM2-deficient cells with compromised CMA activity did not display a noticeable up-regulation of LAMP2A and HSC70 (Fig. 2*D* and *E*) following exposure to the GNPs. Specifically, the increased production of lysosomes induced by GNP^B was found by lysotracker staining (Fig. 2*C*) and flow cytometry (SI Appendix, Fig. S8). The level of LAMP2A in the lysosomal membrane is directly correlated with the CMA activity in intact cells and in isolated lysosomes (45). We found that the amounts of HSC70 and LAMP2A in HeLa cells markedly increased after treatment with GNP^B compared with pristine

GNP (Fig. 2*D*), thereby confirming activation of CMA by GNP^B. This was further demonstrated by western blotting, which revealed elevated expressions of HSC70 and LAMP2A in GNP^B-treated HeLa cells (Fig. 2*E*). However, this phenomenon was not observed in PKM2 knockdown cells. These results clearly demonstrated the proposed mechanism as illustrated in Fig. 2*A*, whereby PKM2 abundantly bound to GNP^{BL} after the NPs escaped from lysosomes (SI Appendix, Fig. S2); subsequently, HSC70 recognized the coronal PKM2 and engaged with the KFERQ-like motif to generate a GNP^{BLC} complex with PKM2 and HSC70 on the surface, and then, the GNP^{BLC} complex bound to other lysosomal membranes via LAMP2A and HSP90, leading to translocation of the complex to the lysosomes. Finally, the whole complex was degraded in the lysosomes, and more lysosomes were produced by the cells to degrade the GNP^{BLC} complex, including remnants of their initial blood corona. We term this process NM-protein corona-induced CMA. PKM2 plays a critical role in the identification of chaperone HSC70 and subsequent enhancement of CMA activity. Moreover, the role of soft corona should also be considered. The soft and hard protein coronas on the surface of nanoparticles may account for roughly a half each in abundance (46). Due to the high affinity of GNP^{BL} and PKM2, more PKM2 may locate in the hard corona based on the Vroman effect. Furthermore, CMA caused by depletion of PKM2 should not be affected by the location of PKM2.

CMA-Induced Changes in Intracellular Protein Homeostasis Perturb Cancer Cell Glycolysis

To gain further insights into the physiological effects arising from increased CMA, we analyzed alterations in key molecular components of cancer cell metabolic processes tightly related to CMA (i.e., glycolysis and lipid metabolism), which have also been identified as the key signaling pathways identified in the cluster II set of coronal proteins (Fig. 1*I*).

We first measured how the concentrations of key components produced in the two processes (glycolysis and lipid metabolism), including glucose, pyruvic acid (PA), lactic acid (LA), and adenosine triphosphate (ATP) concentrations, were affected by GNP and GNP^B exposure. PKM2 knockdown cells (HeLa^{-PKM2}) were used for comparison. We observed that glucose consumption was significantly increased after the HeLa cell exposure to GNP^B, while the corresponding PA and LA concentrations were increased compared with the GNP-exposed and control groups (Fig. 3*A–C*). Meanwhile, more ATP was generated in the GNP^B-treated group to sustain growth of the tumor cells (Fig. 3*D*). These results indicated that GNP^B promoted aerobic glycolysis in the cells. The glycolysis process is highly related to the cellular PKM2 levels. GNP^B bound more PKM2 than pristine GNP after their escape from lysosomes, which induced occurrence of CMA and depleted more PKM2 from the lysosomes. The decreased level of PKM2 then sped up the process of glycolysis and broke down glucose into pyruvate, leading to an overgeneration of ATP (44). This was further demonstrated by comparison with PKM2-deficient cancer cells, where no significant increase of glucose consumption, PA and LA generation, or ATP production was observed. A significantly higher lactate dehydrogenase (LDH) activity was found to accompany the higher concentrations of LA (Fig. 3*E*).

To gain a better understanding of the baseline bioenergetics of HeLa and HeLa^{-PKM2} cells, we further measured extracellular acidification rate (ECAR) to quantify the rate of glycolysis by

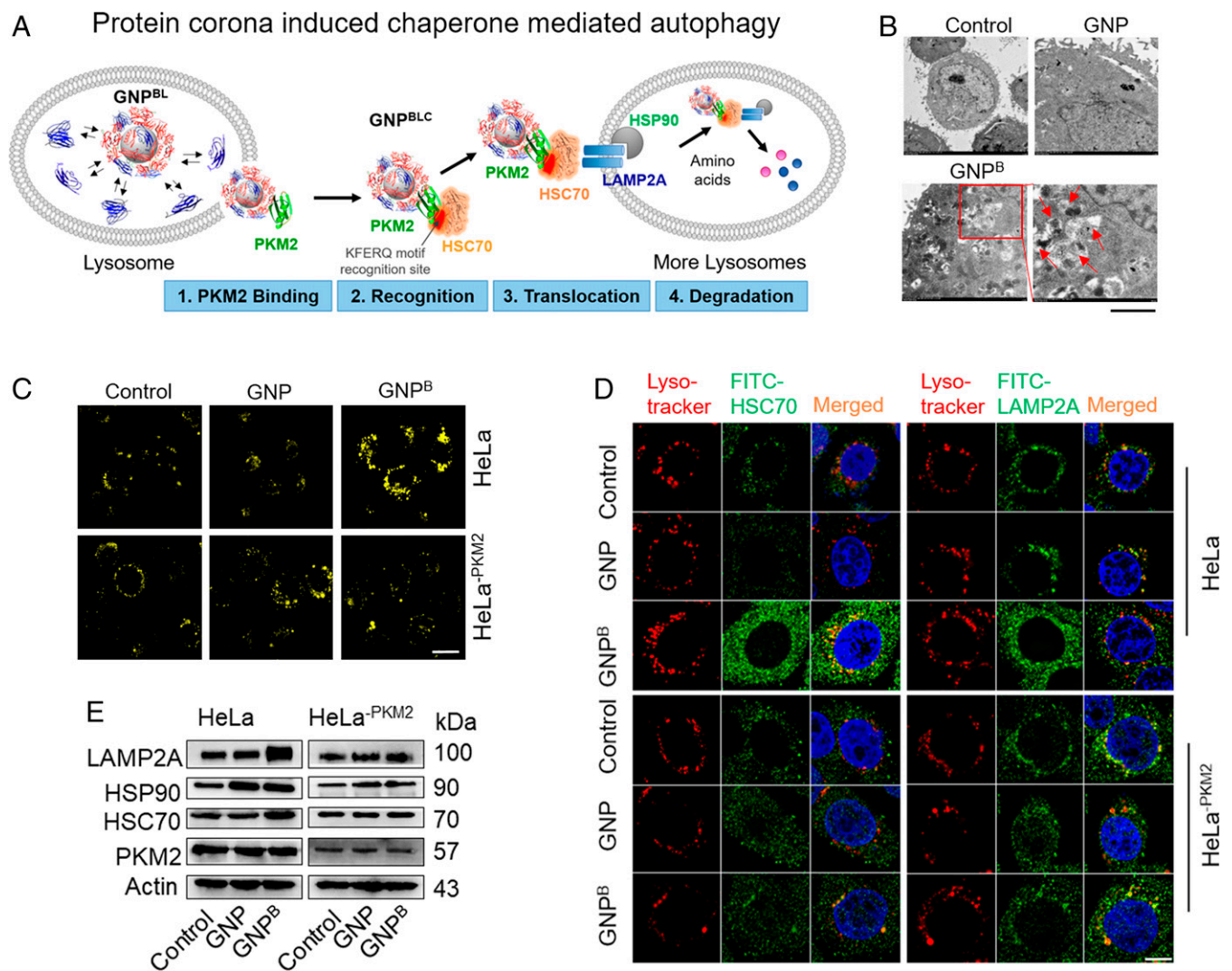


Fig. 2. Proteostasis perturbed by evolution of the intracellular protein corona activates CMA activity. (A) Schematic illustration of the CMA process induced by GNPs depending on their corona composition. (B) TEM image of HeLa cells (control) and HeLa cells that had internalized GNP and GNP^B. Enhanced lysosome storage was found in HeLa cells that had internalized GNP^B (the zoomed-in red box in the GNP^B panel). (Scale bar: 10 μ m.) (C) The lysosomes in HeLa (Upper) and HeLa^{-PKM2} (Lower) were tracked by LysoTracker after treatment with GNP and GNP^B, respectively. (Scale bar: 10 μ m.) (D) HSC70 and LAMP2A expressions in HeLa cells (Upper) and HeLa^{-PKM2} cells (Lower) were detected by laser confocal microscopy. (Scale bar: 10 μ m.) (E) Western blot analysis of CMA activity marker proteins (HSC70, HSP90, and LAMP2A) in HeLa cells (Left) and HeLa cells with PKM2 knocked down (Right; HeLa^{-PKM2} cells).

measuring the dynamics of LA production. We found that the GNP^B-exposed HeLa cells with their enhanced CMA activity showed a rapid increase in ECAR compared with the control and GNP-exposed HeLa cells (Fig. 3F). Next, we added oligomycin to detect the maximal glycolytic capacity. The difference between the maximal glycolytic capacity and the level of basal glycolysis has been defined as the glycolytic reserve. We found that the GNP^B-exposed HeLa cells presented a marked increase in ECAR compared with GNP-exposed HeLa cells (SI Appendix, Fig. S9A), suggesting that GNP^B evoked the glycolytic capacity. However, the ECAR levels in PKM2-deficient cells were almost identical between the GNP and GNP^B treatments (Fig. 3F and G and SI Appendix, Fig. S9B), with no apparent differences between any of the treated groups. Finally, 2-deoxyglucose, a potent glycolysis inhibitor, was added, resulting in all treatment groups showing a rapid drop of ECAR levels in normal cells, while the GNP^B treatment still elicited a higher ECAR level than the other groups in HeLa cells (Fig. 3F and G). Overall, the results demonstrated that GNP^B enhanced the CMA activity and the subsequent glycolytic process under both normal and limited glycolytic machinery conditions.

We next examined the levels of several key glycolytic enzymes that are well-characterized CMA substrates. We observed a marked increase in the messenger RNA (mRNA) levels of 3-phosphoglycerate kinase (PGK1), aldolase (ALDOA), and hexokinase (HK1) in the GNP^B-exposed HeLa cells (Fig. 3H–J). We also found a slight increase of PGK1 and HK1 for the GNP^B-exposed HeLa^{-PKM2} cells (Fig. 3H–J), which revealed that in addition to PKM2, these two enzymes also participated in the CMA process. The higher expressions of HK1 and ALDOA in the GNP^B-exposed HeLa cells were confirmed by western blotting; however, no significant differences were observed in GNP and GNP^B-exposed HeLa^{-PKM2} cells (Fig. 3K). Since some of the glucose was transformed into acetyl-coenzyme A (CoA), a key chemical involved in cellular energy production, we also measured the expression of acetyl-CoA and found a greater expression of acetyl-CoA in GNP^B-exposed HeLa cells than that in GNP-exposed and control HeLa cells (Fig. 3K). This can be attributed to the enhanced CMA activity induced by GNP^B exposure, promoting glycolysis to produce more PA and enhance the citric acid cycle and then, generating more acetyl-CoA flux to the cytosol for lipid synthesis.

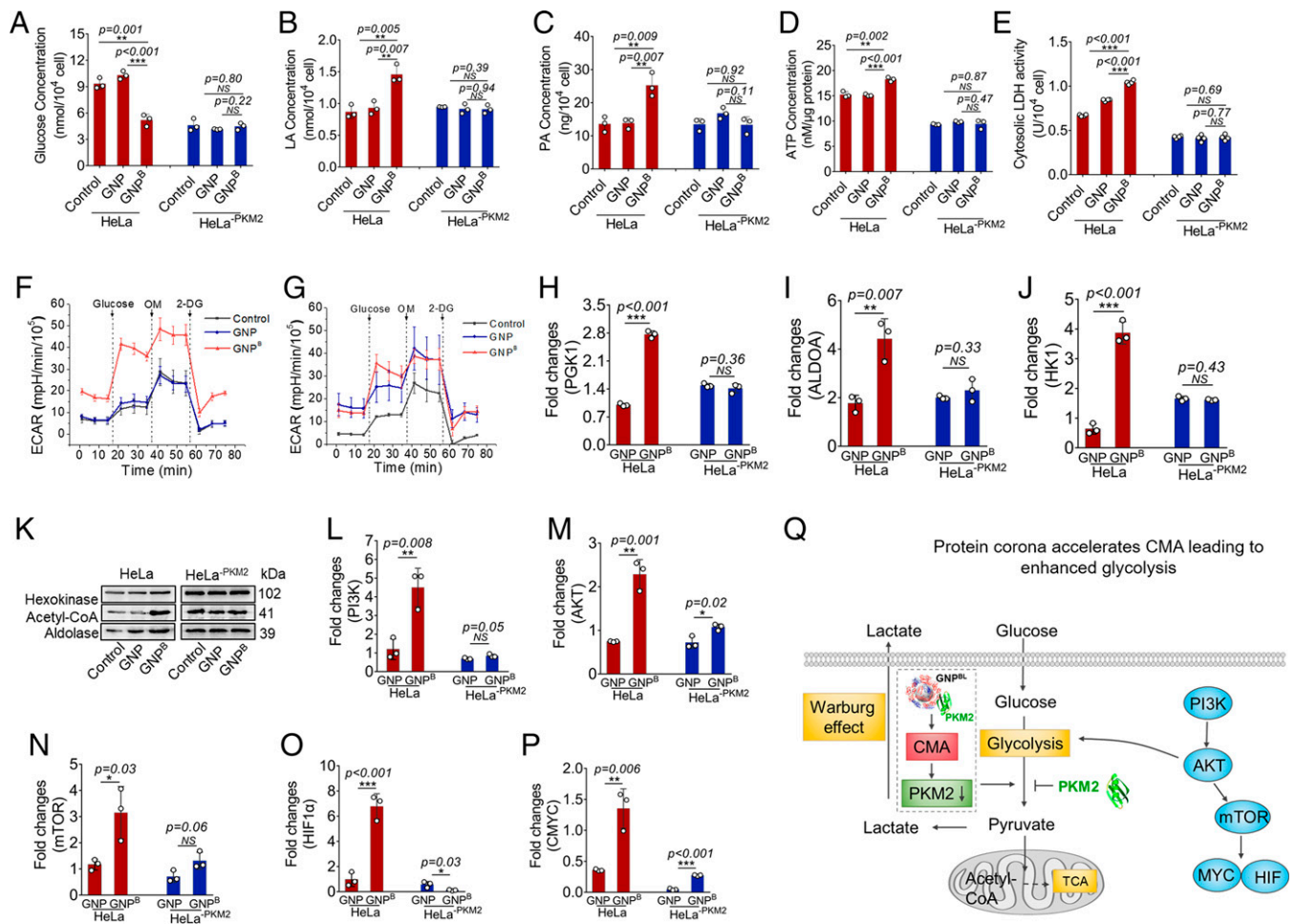


Fig. 3. Increased CMA activity leads to enhanced glycolysis in tumor cells. For the detection of glycolysis, we exposed tumor cells to GNP and GNP^B for 24 h—both HeLa and PKM2 knocked down HeLa cells (HeLa^{PKM2})—with serum-free medium. (A) Quantification of glucose concentration in the whole cellular lysates with the glucose test kit. The lower the glucose concentration, the more it has been consumed by the cells. (B) LA content of the whole cellular lysates was measured using an LA test kit. (C) Pyruvate content of whole-cell lysates was detected with a pyruvate detection kit. (D) ATP content in whole-cell lysates was detected using an ATP detection kit. All values in A–D represent mean \pm SD ($n = 3$). (E) LDH activity in the cytoplasm was detected using an LDH kit, which is a marker enzyme in glycolysis corresponding to the LA concentration. ECAR was monitored using the Seahorse XF24 Extracellular Flux Analyzer in real time for (F) HeLa cells and (G) HeLa^{PKM2} cells. Values represent mean \pm SEM ($n = 3$). 2-DG, 2-deoxyglucose; OM, oligomycin. (H–J) mRNA expression levels of the key enzymes PGK1, ALDOA, and HK1, which were positively correlated with the glycolysis ability ($n = 3$ biologically independent). (K) Western blot analysis of the indicated glycolysis enzymes (HK1, ALDOA) and the generated acetyl-CoA. (L–P) mRNA expression of genes encoding PI3K, AKT, mTOR, HIF1 α , and cMYC, which belong to the PI3K signaling pathway in glycolysis ($n = 3$ biologically replicates). (Q) Schematic illustration of the GNP^B-induced enhancement of CMA-induced glycolysis and the role of the PI3K signaling pathway in this process. TCA, tricarboxylic acid cycle. Data are shown as mean \pm SD ($n = 3$). Statistical significance was tested with a two-tailed, unpaired Student's t test. * $P < 0.05$; ** $P < 0.01$; *** $P < 0.001$. NS, no significance.

In contrast, no obvious differences among groups were found in the HeLa^{PKM2} cells.

The phosphoinositide 3-kinase (PI3K) signaling pathway is closely linked to glucose metabolism (44). In this pathway, PI3K activates protein kinase B (AKT), which stimulates glycolysis by directly regulating glycolytic enzymes and by activating mammalian target of rapamycin (mTOR). mTOR then affects metabolism in a variety of ways (e.g., affecting the glycolytic phenotypes by enhancing hypoxia-inducible factor 1 [HIF1] activity). Cellular-mycelocytomatosis viral oncogene (cMYC) cooperates with HIF1 in activating several genes that encode glycolytic proteins. We found that PI3K expression at the mRNA level was significantly enhanced by fourfold after GNP^B exposure (Fig. 3L). The mRNA levels of AKT, mTOR, HIF1 α , and cMYC in the cells were all markedly up-regulated after GNP^B exposure compared with that after GNP exposure (Fig. 3M–P). These results indicate that the GNP^B-induced CMA activity strengthened and promoted glycolysis through activation of the PI3K–AKT–mTOR–HIF1–cMYC signal pathway (Fig. 3Q).

Enhanced CMA Altered Lipid Metabolism in Tumor Cells

It has been proposed that aerobic glycolysis is the core cellular metabolic process that provides cancer cells with energy and building blocks for macromolecule synthesis, such as carbohydrates, proteins, lipids, and nucleic acids (47). To further investigate the CMA-induced metabolic changes in cancer cells, metabolomics was performed to identify metabolic anomalies and provide quantitative information about the steady-state abundance of intermediates in order to provide an overview of the metabolic network and its perturbation to CMA in cancer cells.

Here, metabolic changes to HeLa cells induced by control, GNP, and GNP^B were determined by LC-MS on positive and negative ion modes. Principal component analysis (PCA) was able to discriminate between GNP^B/control- or GNP^B/GNP-exposed cells, revealing both the original nanoparticles and the protein corona-induced, CMA-induced metabolic changes

(Fig. 4 *A* and *B*). Volcano plots showed significant differences in metabolites between the comparison groups (Fig. 4 *C* and *D*). These altered metabolites were further classified based on the Human Metabolome Database (Fig. 4*E*). The data revealed that most of the changes occurred for lipids and lipids-like molecules, which accounted for 36.6 and 57.1% of the total differential metabolites in the two detection modes, respectively. Moreover, we found that the relative abundances of 3-oxotetradecanoyl-CoA and tetradecanoyl-CoA, which belong to the long-chain fatty acyl-CoA that contributed to lipogenesis, were

significantly increased in the GNP^B treatment groups (Fig. 4 *G* and *H*), which agreed with results above (Fig. 3*K*). These results suggested that CMA-induced collapse of cancer cell metabolism occurred mainly by disruption of lipid metabolism following release of blood proteins intracellularly from the GNP corona.

In addition, a comprehensive bioinformatic pathway analysis was carried out for the differentially expressed metabolites based on the Kyoto Encyclopedia of Genes and Genomes (KEGG) pathway database. We observed that the altered metabolites were mostly

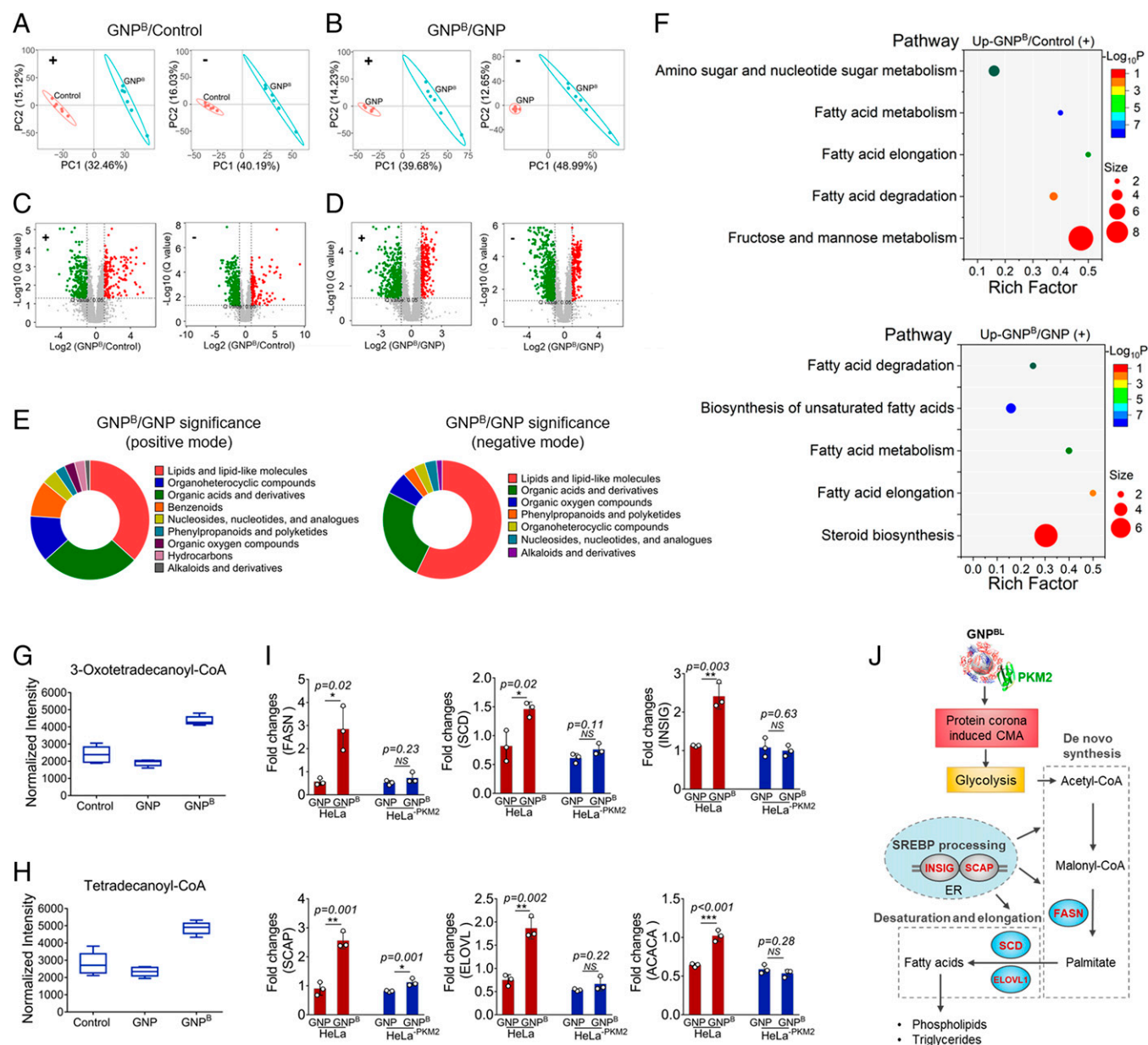


Fig. 4. Metabolomic analysis of enhancement of CMA and consequent promotion of changes in tumor cell metabolism. HeLa cells were treated with GNP and GNP^B for 24 h and then, collected for metabolomic detection by LC-MS. (A) PCA of the GNP^B vs. control (GNP^B/control) in positive-ion (Left) and negative-ion (Right) modes, respectively ($n = 6$ for each individual group). +, positive-ion mode; -, negative-ion mode. (B) PCA of GNP^B vs. GNP (GNP^B/GNP) in positive-ion (Left) and negative-ion (Right) modes, respectively ($n = 6$ for each individual group). (C) Volcano map of the difference analysis of GNP^B and control groups. (Left) Positive-ion mode. (Right) Negative mode ($n = 6$). (D) Volcano map of the difference analysis of GNP^B and GNP groups ($n = 6$). (E) Relative abundance of metabolites categories with significant differences between GNP^B vs. GNP (GNP^B/GNP; $n = 6$ for each individual group). (F) Significant enrichment analysis of corresponding pathways with KEGG pathway enrichment analysis for the GNP^B vs. control groups and GNP^B vs. GNP groups. +, positive-ion mode. (G) Relative abundance of the 3-oxotetradecanoyl-CoA and (H) tetradecanoyl-CoA based on the metabolomics as determined by LC-MS. (I) Expression levels of ELOVL1, FASN, INSIG1, SCAP, and SCD mRNA were quantified by real-time PCR, indicating that multiple lipid metabolism-regulating genes were up-regulated with the increased CMA activity ($n = 3$ biologically independent). Data are shown as mean \pm SD. Statistical significance was tested with a two-tailed, unpaired Student's *t* test. * $P < 0.05$; ** $P < 0.01$; *** $P < 0.001$. NS, no significance. (J) Schematic illustration of evolution of the intracellular protein corona from blood plasma to cytoplasm, which resulted in enhanced CMA activity of cancer cells, affecting the glycolytic process and further accelerating lipid metabolism. ER, endoplasmic reticulum.

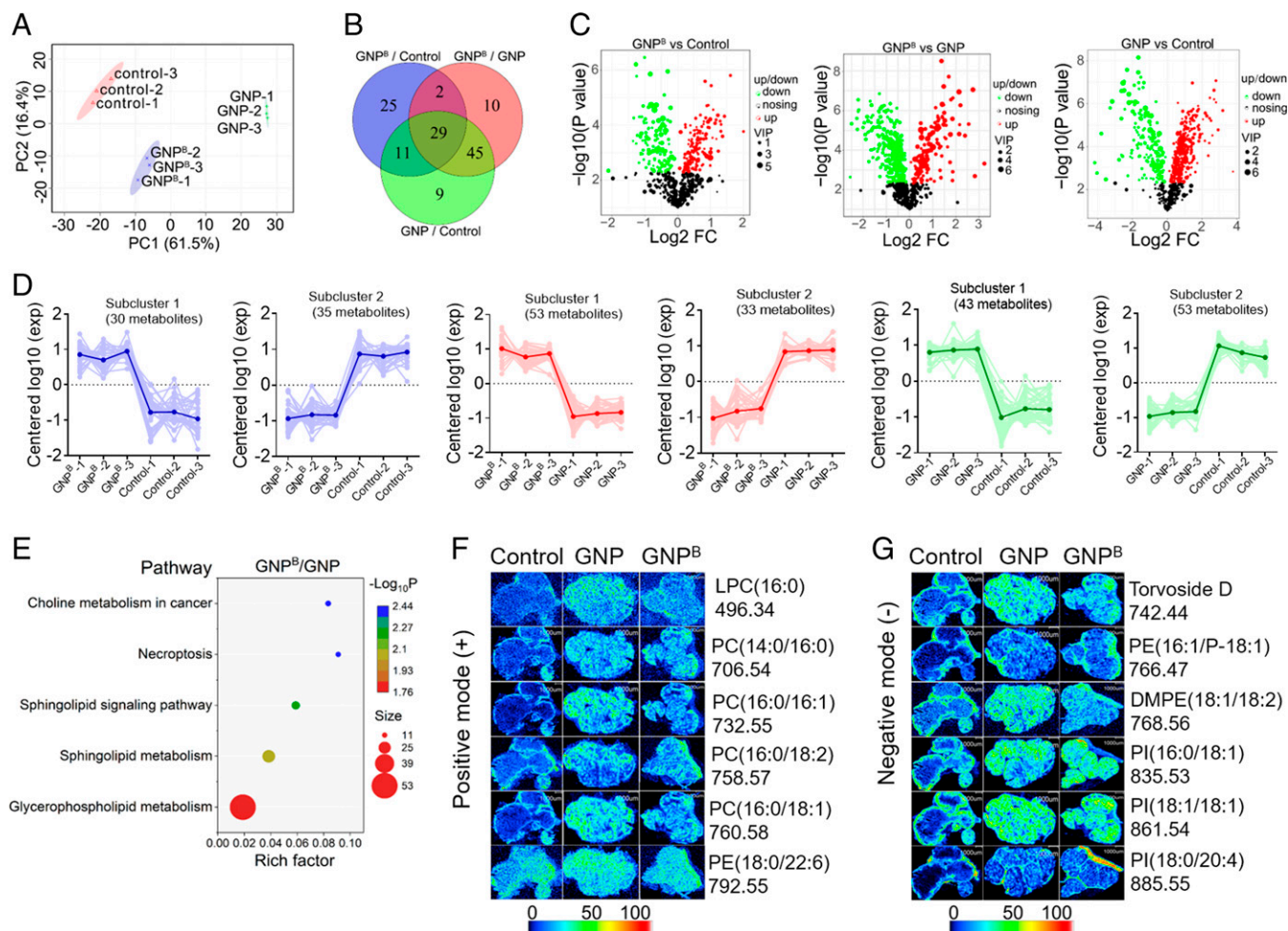


Fig. 5. Lipid metabolomics analysis of the enhancement of CMA, which promotes changes in tumor tissue metabolism. HeLa cells were subcutaneously inoculated in BALB/C female nude mice, and GNP and GNP^B were administered intratumorally twice at days 7 and 9 (*n* = 3 for each group). Tumor tissues were collected for nontargeted lipidomic analysis based on LC-MS. (A) PCA for the three tumor tissue groups, indicating differences between control, GNP, and GNP^B treatments. PC, principal component. (B) A comparative analysis of the differentially expressed metabolites was summarized in a Venn diagram, with each circle representing one of the treatment groups, the number in the circle representing the number of unique metabolites, and the numbers in the overlaps representing the number of common or shared metabolites. (C) Volcano plots of the differentially expressed metabolites in the indicated groups using a Student's *t* test combined with multivariate analysis of the orthogonal partial least squares discrimination analysis (OPLS-DA) method to screen the differences between groups of metabolites (that meet the condition of variable importance in projection VIP > 1; *P* value < 0.05). FC, fold change; VIP, variable importance in projection. (D) Cluster trend lines in which the expression trend of each subcluster is presented as a broken line chart. The x axis indicates the sample group, and the y axis shows the amount of the metabolites expressed. Each gray line represents a metabolite, and the bright lines represent an average expression of all metabolites in the subcluster. Each figure shows one type of expression pattern: that is, the trend of changes in the expression of metabolites in this group. (E) A bubble diagram of the KEGG pathway enrichment analysis of different metabolites in the GNP and GNP^B groups. The colors indicate the significance of enrichment, with a darker color indicating a more significant enrichment of the pathway, while the color gradient on the right indicates the *P* value. (F and G) Representative imaging mass spectrometry analysis showing the spatial distribution of apparently highly expressed lipid components in the tumor slices. (Scale bars: 1 mm.)

enriched in the fatty acid synthesis- and metabolism-related pathways, including biosynthesis of unsaturated fatty acids, fatty acid elongation, and degradation (Fig. 4F). Enhanced lipogenesis in cancer cells is caused by up-regulation of lipid-metabolizing enzymes (48). Acetyl-CoA carboxylase A produces malonyl-CoA, which is used by fatty acid synthase (FASN) to produce palmitate *de novo*. The produced fatty acids can be elongated by elongases such as ELOVL1 (elongation of very long-chain fatty acid-like 1), an elongating saturated lipid, and/or desaturated by desaturases such as SCD (stearoyl-CoA desaturase). In addition, insulin-induced gene 1 (INSIG1) and sterol regulatory element-binding protein cleavage-activating protein (SCAP) participate in lipid metabolism regulation (49). Thus, to confirm the effect of GNP^B on promoting fatty acid metabolism, the expression of genes related to fatty acid biosynthesis, elongation, and degradation were quantified by real-time PCR as shown in Fig. 4I. Expressions of FASN, SCD, INSIG, SCAP, and ELOVL mRNA were exclusively increased after GNP^B exposure, and this was not observed

in HeLa^{-PKM2} cells, suggesting that GNP^B promoted synthesis of fatty acids. Taken together, our results indicated that evolution of the protein corona as the GNP passed from blood plasma to cytoplasm and the resulting intracellular exchange of corona proteins, which led to shedding of blood proteins inside the cell, enhanced the CMA activity of HeLa cells, thereby affecting the glycolytic process and further accelerating lipid metabolism as illustrated in Fig. 4J.

Demonstration of CMA-Mediated Lipid Metabolic Alteration at the Tissue Level

Measuring lipid species and their metabolism and understanding the pathways involved are crucial to fully understand cellular metabolism. Almost 30% of the proteins identified as CMA substrates participate in lipid metabolism, predominantly in triglyceride synthesis, steroid metabolism, and lipid binding and transport (50, 51). Deficiency in CMA promotes lipid accumulation in

Intracellular nanoparticle-protein corona triggers CMA

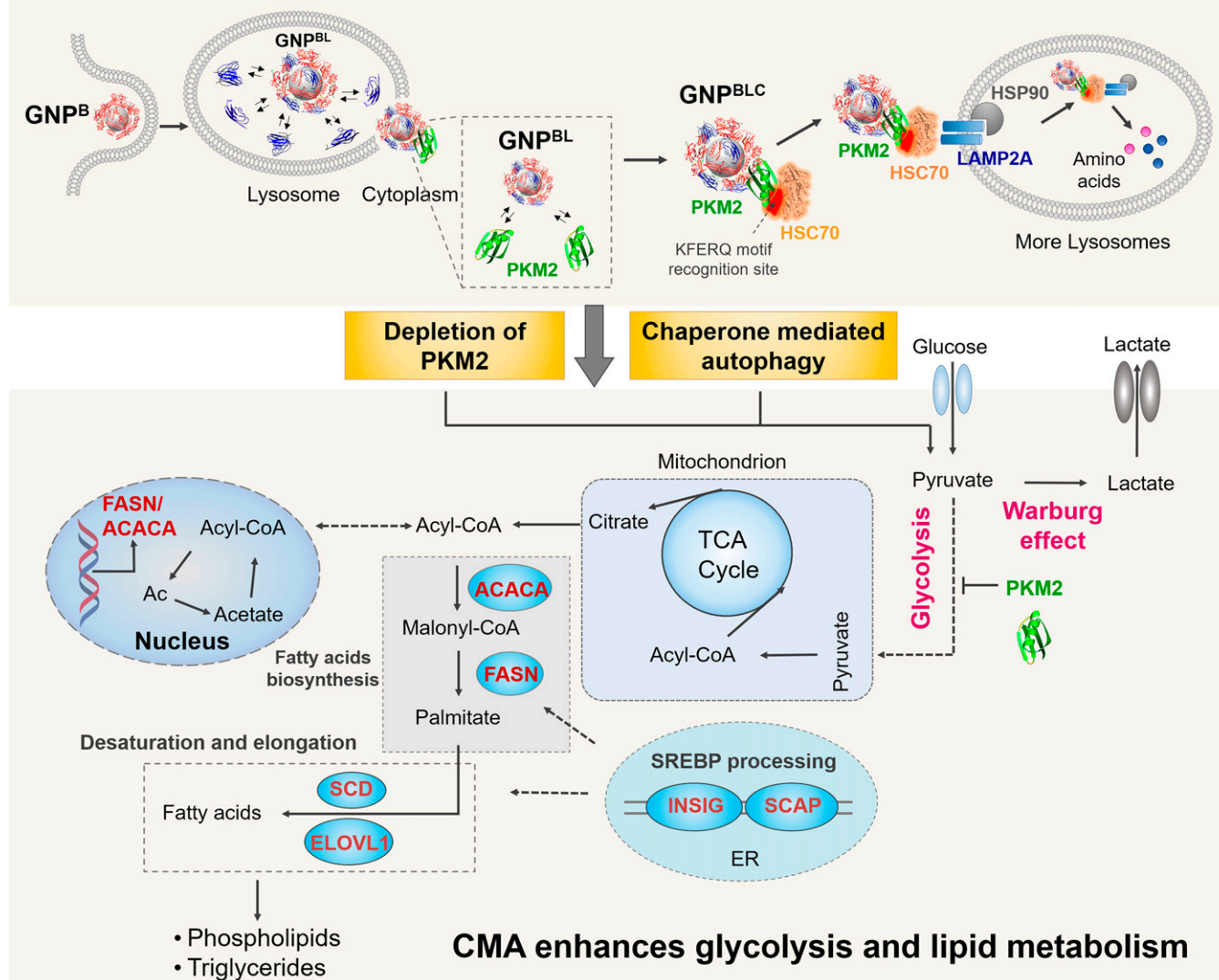


Fig. 6. Schematic illustration of evolution of the GNP-protein corona from the blood to the intracellular space and the exchange with cellular proteins and chaperones triggering an elevated CMA activity, which selectively remodels cellular metabolism. ACACA, acetyl-CoA carboxylase A; TCA, tricarboxylic acid cycle.

macrophages potentially through regulating enzymes involved in lipid metabolism (52). Lipidomics enables large-scale study of lipids using the principles of analytical chemistry (53). To verify the effect of GNP^B-induced CMA activity enhancement on tumor lipid metabolism, lipidomics detection was performed at the tumor tissue level in this study. We first established the tumor model by inoculating HeLa cells subcutaneously in mice, administered GNP and GNP^B into the tumor tissue intratumorally, and then, collected tumor tissues for lipidomics using ultraperformance LC-MS.

The PCA score plot showed a clear separation between all groups, indicating that GNP and GNP^B treatments caused different perturbations in the lipidomic profiles in the tumor tissues (Fig. 5A and *SI Appendix*, Fig. S10). In total, 94 and 67 lipids were significantly altered by the GNP and GNP^B treatments, respectively. Presence of the plasma protein corona on the GNPs significantly altered 86 lipids (Fig. 5B). Twenty-nine lipids overlapped among the treatments and control groups, as detailed in *SI Appendix*, Table S3. The volcano plot (Fig. 5C) showed that the numbers of up- and down-regulated lipids were almost similar in all paired groups. A full list of

significantly changed lipids in GNP^B/control and GNP^B/GNP is provided in *SI Appendix*, Table S4.

We next analyzed the cluster trend lines for the differentially expressed lipids as shown in Fig. 5D. We found that the amounts of up-/down-regulated lipid metabolites were similar for the GNP^B/control comparison groups at 30 and 35, respectively. The 53 lipids displayed in subcluster 1 showed an obvious up-regulation with GNP^B/GNP, while 33 lipids belonging to subcluster 2 showed a clear downward trend, indicating the effect of the protein corona on lipid metabolism. In addition, exposure of GNPs promoted the up-regulation of 43 lipids and down-regulated 53 lipids. Detailed information on the metabolites is listed in *SI Appendix*, Tables S5–S7. KEGG pathway enrichment analysis showed that the significantly differently expressed lipids were mostly enriched in glycerophospholipid and sphingolipid metabolism pathways (Fig. 5E). Additionally, choline metabolism in the cells was changed significantly, which revealed that the syntheses of phosphatidylcholine and sphingomyelin were affected by the GNP^B exposure.

Matrix-assisted laser desorption/ionization–mass spectrometry imaging is an advanced technique that combines mass

spectrometry and imaging that are capable of obtaining the spatial distribution (spatial resolution down to 20 μm) of molecules, such as proteins, peptides, lipids, drugs, and metabolites, in a single tissue of interest (54–56). Using this technique, we evaluated spatial distribution of significantly changed lipids as detected by the lipidomics. In the positive-ion mode (Fig. 5F), we found that the spatial distributions of lysophosphatidylcholine(16:0), phosphatidylcholine (PC)(16:0/16:1), and PC(16:0/18:1) as well as phosphatidylethanolamine (PE)(18:0/22:6) were quite extensive in the GNP treatment group compared with the control and GNP^B groups. Notably, the invasion of the GNPs resulted in a large distribution of PC(14:0/16:0), PC(16:0/16:1), PC(16:0/18:2), and PC(16:0/18:0) within the tumors, while they were mainly distributed in the tumor epidermis in the controls groups. PE(18:0/22:6) was distributed in the inner tumor in the untreated control, but the intensity increased rapidly after injection of the GNPs and GNP^B. In parallel, we observed bountiful phosphatidyl-inositol (PI)(16:0/18:1) and PI(18:1/18:1) spread throughout the whole tumor tissue after treatment with GNP and GNP^B during the negative-ion mode imaging (Fig. 5G). Specially, Torvoside D and phosphoethanolamine(18:1/18:2) increased remarkably following the GNP exposure. In addition, PE(16:1/18:1) and PI(18:0/20:4) were expressed significantly more at the epidermic tumor tissues following GNP^B exposure. Taken together, we concluded that the GNPs significantly disrupted metabolism of tumor tissues and promoted synthesis of phospholipids compared with the untreated control group.

Conclusions

In summary, this study revealed a previously unknown effect of intracellular exchange of protein corona components on CMA activation as a result of proteostasis disruption. The enhanced CMA activity arising from shedding of blood proteins intracellularly was further identified by determining the cellular metabolism at both cellular and tissue levels (Fig. 6). In brief, as nanoparticles migrated from the bloodstream into cells, the nanoparticles would disassociate part of their acquired blood proteins, which were replaced by cellular proteins due to their higher affinity for the nanoparticles' surface. This intracellular transformation of the protein corona further modulated nanoparticle-induced biological processes, including proteostasis and metabolic stress responses, especially glycolysis and lipid metabolism. This alteration of cell metabolism was caused by the interplay of coronal proteins with other molecules in the cellular environments. PKM2, a key molecule for cellular metabolism, was incorporated into the nanoparticles corona and subsequently dominated their biological identity.

For NMs used as nanomedicines or nanocarriers, a better understanding of the "biological identity" of their intracellular protein corona is crucial to ensure their biological benefits while minimizing their potential hazards. Biologically, proteostasis is central to cell function, and its disruption, as revealed by the current study, entails profound implications for

mediating human disorders ranging from cancers to aging. Furthermore, the protein corona-induced CMA can influence cellular clearance of nanoparticles and alter cellular metabolism, which may impact the efficiency and bioavailability of nanoscale delivery systems. CMA could be a useful target for directing and manipulating the cellular and subcellular fate of nanoparticles. Such understanding of the intracellular protein corona, together with our existing knowledge of the physical and biochemical transformations of NMs in tissues and organs (11, 57, 58), highlights the complexity of the nano–bio interface and provides a crucial new molecular insight for guiding the safe design of future nanomedicines.

Materials and Methods

We include the detailed information of the materials and methods in [SI Appendix](#), specifically synthesis and characterization of GNPs, human blood plasma preparation and extraction of cytosol and lysosomes from HeLa cells, formation of GNP-corona complexes, liquid chromatography-mass spectrometry/mass spectrometry quantification for proteomics, cellular localization of GNPs and GNP-corona complexes, cellular metabolism, and MST measurement as well as statistical analysis. This study was approved by the Chinese People's Liberation Army General Hospital Ethics Committee, and informed consent was obtained from all donors.

Data Availability. The metabolomics and lipidomics data have been deposited in MetaboLights and are accessible via accession nos. [MTBLS4884](#) and [MTBLS4887](#). All study data are included in the article and/or [SI Appendix](#).

ACKNOWLEDGMENTS. This work was financially supported by the Key Program for International S&T Cooperation Projects of China (Grants 2021YFE0112600 and 2020YFA0710702), the National Key R&D Program of China (Grant 2021YFA1200900), the National Natural Science Foundation of China (Grants 32071402 and 20207810), the Science Fund for Creative Research Groups of the National Natural Science Foundation of China (Grant 11621505), the Strategic Priority Research Program of Chinese Academy of Sciences (Grant XDB36000000), the Research and Development Project in Key Areas of Guangdong Province (Grant 2019B090917011), and by Royal Society International Exchanges 2018 Cost Share (China) Grant IEC\NSFC\181712. I.L., P.Z., Z.G., and A.J.C. acknowledge support from the University of Birmingham's Institute of Global Innovation via the Environmental Pollution Solutions theme and funding from European Union Horizon 2020 Projects ACEnano (Grant Agreement No. H2020-NMBP-2016-720952), NanoCommons (Grant Agreement No. 731032), and NanoSolveIT (Grant Agreement No. 814572). We greatly appreciate the support of Dr. Jing Wang, Dr. Qian Wang, and Dr. Wenzhe Li from the State Key Laboratory of Natural and Biomimetic Drugs at Peking University. We also thank Dr. Bozhong Tang from the Shimadzu China Mass Spectrometry Platform.

Author affiliations: ^aChinese Academy of Sciences Key Laboratory of Biomedical Effects of Nanomaterials and Nanosafety, National Center for Nanoscience and Technology, Beijing 100190, China; ^bChinese Academy of Sciences Center for Excellence in Nanoscience, National Center for Nanoscience and Technology, Beijing 100190, China; ^cSchool of Nano Science and Technology, University of Chinese Academy of Sciences, Beijing 101400, China; ^dNational Laboratory of Biomacromolecules, Institute of Biophysics, Chinese Academy of Sciences, Beijing 100101, China; ^eThe GBA National Institute for Nanotechnology Innovation, Guangzhou 510700, China; and ^fSchool of Geography, Earth and Environmental Sciences, University of Birmingham, Birmingham B15 2TT, United Kingdom

1. D. Docter *et al.*, The nanoparticle biomolecule corona: Lessons learned—challenge accepted? *Chem. Soc. Rev.* **44**, 6094–6121 (2015).
2. T. Cedervall *et al.*, Understanding the nanoparticle-protein corona using methods to quantify exchange rates and affinities of proteins for nanoparticles. *Proc. Natl. Acad. Sci. U.S.A.* **104**, 2050–2055 (2007).
3. I. Lynch, K. A. Dawson, Protein-nanoparticle interactions. *Nano Today* **3**, 40–47 (2008).
4. E. Mahon, A. Salvati, F. Baldelli Bombelli, I. Lynch, K. A. Dawson, Designing the nanoparticle-biomolecule interface for "targeting and therapeutic delivery." *J. Control. Release* **161**, 164–174 (2012).
5. S. Schöttler *et al.*, Protein adsorption is required for stealth effect of poly(ethylene glycol)- and poly(phosphoester)-coated nanocarriers. *Nat. Nanotechnol.* **11**, 372–377 (2016).
6. K. Saha *et al.*, Regulation of macrophage recognition through the interplay of nanoparticle surface functionality and protein corona. *ACS Nano* **10**, 4421–4430 (2016).
7. R. Cai *et al.*, Corona of thorns: The surface chemistry-mediated protein corona perturbs the recognition and immune response of macrophages. *ACS Appl. Mater. Interfaces* **12**, 1997–2008 (2020).
8. A. Salvati *et al.*, Transferrin-functionalized nanoparticles lose their targeting capabilities when a biomolecule corona adsorbs on the surface. *Nat. Nanotechnol.* **8**, 137–143 (2013).
9. J. Y. Oh *et al.*, Cloaking nanoparticles with protein corona shield for targeted drug delivery. *Nat. Commun.* **9**, 4548 (2018).
10. N. Bertrand *et al.*, Mechanistic understanding of in vivo protein corona formation on polymeric nanoparticles and impact on pharmacokinetics. *Nat. Commun.* **8**, 777 (2017).

11. M. Cao *et al.*, Molybdenum derived from nanomaterials incorporates into molybdenum enzymes and affects their activities in vivo. *Nat. Nanotechnol.* **16**, 708–716 (2021).
12. Z. J. Deng, M. Liang, M. Monteiro, I. Toth, R. F. Minchin, Nanoparticle-induced unfolding of fibrinogen promotes Mac-1 receptor activation and inflammation. *Nat. Nanotechnol.* **6**, 39–44 (2011).
13. V. P. Vu *et al.*, Immunoglobulin deposition on biomolecule corona determines complement opsonization efficiency of preclinical and clinical nanoparticles. *Nat. Nanotechnol.* **14**, 260–268 (2019).
14. D. Baimanov *et al.*, Immunological responses induced by blood protein coronas on two-dimensional MoS₂ nanosheets. *ACS Nano* **14**, 5529–5542 (2020).
15. M. Guo *et al.*, The underlying function and structural organization of the intracellular protein corona on graphdiyne oxide nanosheet for local immunomodulation. *Nano Lett.* **21**, 6005–6013 (2021).
16. Z. Wang *et al.*, Specifically formed corona on silica nanoparticles enhances transforming growth factor β 1 activity in triggering lung fibrosis. *ACS Nano* **11**, 1659–1672 (2017).
17. H. Yin *et al.*, Reducing the cytotoxicity of ZnO nanoparticles by a pre-formed protein corona in a supplemented cell culture medium. *RSC Advances* **5**, 73963–73973 (2015).
18. C. Ge *et al.*, Binding of blood proteins to carbon nanotubes reduces cytotoxicity. *Proc. Natl. Acad. Sci. U.S.A.* **108**, 16968–16973 (2011).
19. L. Wang *et al.*, Revealing the binding structure of the protein corona on gold nanorods using synchrotron radiation-based techniques: Understanding the reduced damage in cell membranes. *J. Am. Chem. Soc.* **135**, 17359–17368 (2013).
20. J. Ren *et al.*, Precision nanomedicine development based on specific opsonization of human cancer patient-personalized protein coronas. *Nano Lett.* **19**, 4692–4701 (2019).
21. N. Gong *et al.*, Carbon-dot-supported atomically dispersed gold as a mitochondrial oxidative stress amplifier for cancer treatment. *Nat. Nanotechnol.* **14**, 379–387 (2019).
22. D. B. Thimiri Govinda Raj, N. A. Khan, Surface functionalization dependent subcellular localization of superparamagnetic nanoparticle in plasma membrane and endosome. *Nano Converg.* **5**, 4 (2018).
23. D. Liße *et al.*, Engineered ferritin for magnetogenetic manipulation of proteins and organelles inside living cells. *Adv. Mater.* **29**, 1700189 (2017).
24. C. D. Dekiwadia, A. C. Lawrie, J. V. Fecondo, Peptide-mediated cell penetration and targeted delivery of gold nanoparticles into lysosomes. *J. Pept. Sci.* **18**, 527–534 (2012).
25. A. M. Billing *et al.*, Fast and robust proteome screening platform identifies neutrophil extracellular trap formation in the lung in response to cobalt ferrite nanoparticles. *ACS Nano* **14**, 4096–4110 (2020).
26. A. O. Khan *et al.*, Surface chemistry-dependent evolution of the nanomaterial corona on TiO₂ nanomaterials following uptake and sub-cellular localization. *Nanomaterials (Basel)* **10**, 401 (2020).
27. M. Qin *et al.*, Proteomic analysis of intracellular protein corona of nanoparticles elucidates nano-trafficking network and nano-bio interactions. *Theranostics* **10**, 1213–1229 (2020).
28. R. Cai, C. Chen, The crown and the scepter: Roles of the protein corona in nanomedicine. *Adv. Mater.* **31**, e1805740 (2018).
29. Y. Wang, R. Cai, C. Chen, The Nano-Bio interactions of nanomedicines: Understanding the biochemical driving forces and redox reactions. *Acc. Chem. Res.* **52**, 1507–1518 (2019).
30. P. Chen *et al.*, Amyloidosis inhibition, a new frontier of the protein corona. *Nano Today* **35**, 100937 (2020).
31. Y. Liu *et al.*, Nano-bio interactions in cancer: From therapeutics delivery to early detection. *Acc. Chem. Res.* **54**, 291–301 (2021).
32. E. T. Powers, W. E. Balch, Diversity in the origins of proteostasis networks—a driver for protein function in evolution. *Nat. Rev. Mol. Cell Biol.* **14**, 237–248 (2013).
33. C. Hetz, F. R. Papa, The unfolded protein response and cell fate control. *Mol. Cell* **69**, 169–181 (2018).
34. X. Wang *et al.*, Chiral surface of nanoparticles determines the orientation of adsorbed transferrin and its interaction with receptors. *ACS Nano* **11**, 4606–4616 (2017).
35. F. Wang *et al.*, The biomolecular corona is retained during nanoparticle uptake and protects the cells from the damage induced by cationic nanoparticles until degraded in the lysosomes. *Nanomedicine* **9**, 1159–1168 (2013).
36. S. Dominguez-Medina *et al.*, Adsorption and unfolding of a single protein triggers nanoparticle aggregation. *ACS Nano* **10**, 2103–2112 (2016).
37. B. Lu, S. Guo, Mechanisms linking mitochondrial dysfunction and proteostasis failure. *Trends Cell Biol.* **30**, 317–328 (2020).
38. Z. Dong, H. Cui, The autophagy-lysosomal pathways and their emerging roles in modulating proteostasis in tumors. *Cells* **8**, 4 (2018).
39. P. C. Ke *et al.*, Half a century of amyloids: Past, present and future. *Chem. Soc. Rev.* **49**, 5473–5509 (2020).
40. S. Kaushik, A. M. Cuervo, The coming of age of chaperone-mediated autophagy. *Nat. Rev. Mol. Cell Biol.* **19**, 365–381 (2018).
41. M. Kon *et al.*, Chaperone-mediated autophagy is required for tumor growth. *Sci. Transl. Med.* **3**, 109ra117 (2011).
42. F. Bertoli, D. Garry, M. P. Monopoli, A. Salvati, K. A. Dawson, The intracellular destiny of the protein corona: A study on its cellular internalization and evolution. *ACS Nano* **10**, 10471–10479 (2016).
43. L. Lv *et al.*, Acetylation targets the M2 isoform of pyruvate kinase for degradation through chaperone-mediated autophagy and promotes tumor growth. *Mol. Cell* **42**, 719–730 (2011).
44. R. A. Cairns, I. S. Harris, T. W. Mak, Regulation of cancer cell metabolism. *Nat. Rev. Cancer* **11**, 85–95 (2011).
45. T. Saha, LAMP2A overexpression in breast tumors promotes cancer cell survival via chaperone-mediated autophagy. *Autophagy* **8**, 1643–1656 (2012).
46. X. Tan, K. Welscher, Particle-by-particle in situ characterization of the protein corona via real-time 3D single-particle-tracking spectroscopy. *Angew. Chem. Int. Ed. Engl.* **60**, 22359–22367 (2021).
47. M. G. Vander Heiden, L. C. Cantley, C. B. Thompson, Understanding the Warburg effect: The metabolic requirements of cell proliferation. *Science* **324**, 1029–1033 (2009).
48. F. Röhrig, A. Schulze, The multifaceted roles of fatty acid synthesis in cancer. *Nat. Rev. Cancer* **16**, 732–749 (2016).
49. M. Hilvo *et al.*, Novel theranostic opportunities offered by characterization of altered membrane lipid metabolism in breast cancer progression. *Cancer Res.* **71**, 3236–3245 (2011).
50. S. Kaushik, A. M. Cuervo, Degradation of lipid droplet-associated proteins by chaperone-mediated autophagy facilitates lipolysis. *Nat. Cell Biol.* **17**, 759–770 (2015).
51. J. L. Schneider, Y. Suh, A. M. Cuervo, Deficient chaperone-mediated autophagy in liver leads to metabolic dysregulation. *Cell Metab.* **20**, 417–432 (2014).
52. L. Qiao *et al.*, Deficient chaperone-mediated autophagy promotes lipid accumulation in macrophage. *J. Cardiovasc. Transl. Res.* **14**, 661–669 (2021).
53. X. Han, Lipidomics for studying metabolism. *Nat. Rev. Endocrinol.* **12**, 668–679 (2016).
54. S. Meding, A. Walch, MALDI imaging mass spectrometry for direct tissue analysis. *Methods Mol. Biol.* **931**, 537–546 (2013).
55. E. R. Amstalden van Hove *et al.*, Multimodal mass spectrometric imaging of small molecules reveals distinct spatio-molecular signatures in differentially metastatic breast tumor models. *Cancer Res.* **70**, 9012–9021 (2010).
56. K. E. Burnum *et al.*, Spatial and temporal alterations of phospholipids determined by mass spectrometry during mouse embryo implantation. *J. Lipid Res.* **50**, 2290–2298 (2009).
57. X. Li *et al.*, Navigating metabolic pathways to enhance antitumour immunity and immunotherapy. *Nat. Rev. Clin. Oncol.* **16**, 425–441 (2019).
58. X. Jiang, B. Du, J. Zheng, Glutathione-mediated biotransformation in the liver modulates nanoparticle transport. *Nat. Nanotechnol.* **14**, 874–882 (2019).